Generalized phase-space tomography for intense beams[a)]

D. Stratakis,[1,b)] R. A. Kishek,[2] S. Bernal,[2] R. B. Fiorito,[2] I. Haber,[2] M. Reiser,[2] P. G. O'Shea,[2] K. Tian,[3] and J. C. T. Thangaraj[4]
[1]*Department of Physics, Brookhaven National Laboratory, Upton, New York 11973, USA*
[2]*Institute for Research in Electronics and Applied Physics, University of Maryland, College Park, Maryland 20742, USA*
[3]*Thomas Jefferson National Accelerator Facility, Newport News, Virginia 23606, USA*
[4]*Fermi National Accelerator Laboratory, Batavia, Illinois 60510, USA*

(Received 21 November 2009; accepted 27 December 2009; published online 12 February 2010)

Tomographic phase-space mapping in an intense particle beam is reviewed. The diagnostic is extended to beams with space-charge by assuming linear forces and is implemented using either solenoidal or quadrupole focusing lattices. The technique is benchmarked against self-consistent simulation and against a direct experimental sampling of phase-space using a pinhole scan. It is demonstrated that tomography can work for time-resolved phase-space mapping and slice emittance measurement. The technique is applied to a series of proof-of-principle tests conducted at the University of Maryland. © *2010 American Institute of Physics*. [doi:10.1063/1.3298894]

I. INTRODUCTION

Maintaining and preserving a high density of particles in phase-space is an important requirement for beams of many accelerator applications. Examples of those include accelerator-driven neutron sources,[1] high luminosity high-energy colliders,[2] free-electron lasers,[3] energy-recovery linacs,[4] and heavy-ion inertial fusion (HIF) drivers.[5] At the low-energy end of these accelerators, the particle dynamics can be significantly affected by their mutual repulsion, also known as space-charge.[6] Space-charge can engender collective behavior[7] and is often destructive to the beam.[8,9] For instance, space-charge can cause halo formation[10] which can result to beam losses and activation of the machine. Therefore, having a good understanding of beams with space-charge is necessary, and phase-space reconstruction is an important tool in achieving this goal.

Tomographic techniques previously have shown success in reconstructing the phase-space distribution. Computerized tomography is well known in the medical community and was originally developed to process x-ray images. A Norwegian physicist Abel (1826) first formulated the concept of tomography[11] for an object with axisymmetric geometry. Nearly 100 years later, an Austrian mathematician Radon (1917) developed a theorem extending the idea to arbitrarily shaped objects; it stated that an object in an n-dimensional space can be recovered from a sufficient number of projections on to $(n-1)$-dimensional space.[12]

In beam physics, we can map the phase-space using information taken from the distribution of spatial density at the same point. A simple scaling equation relates the spatial beam projections to the Radon transform of the transverse-phase space, as demonstrated in the 1970s by Sander *et al.*[13] Specifically, the authors imaged the beam at different positions along the beam line and then reconstructed the phase-space distribution using tomographic computer programs. The unavailability of profile monitors along the beam line limited these spatial projections to three; therefore, the resolution of the reconstructed phase space was sparse. Similarly, Fraser[14] reconstructed the phase space by tomography via either two or three projections. Again, with so few views, the phase-space plots lacked structure.

Phase-space tomography was implemented with greater accuracy by the study of McKee *et al.*[15] wherein they combined the ideas of tomography with quadrupole scanning to recover density information in phase space. To account for beam stretching while scanning the magnet, these researchers scaled the profiles using a scaling parameter. McKee *et al.* demonstrated that both the scaling parameter and the angle of projection can be calculated from the beam's transport matrix. Since then, several authors adopted a similar approach.[16–20]

We note that all these tomography studies were applied to relativistic beams, and the tomography algorithm did not consider space-charge forces. In this work a model is presented to apply tomography to beams with space charge. The technique is generalized to account for both solenoidal- and quadrupole-focusing lattices. The method is benchmarked by computer simulation and a pinhole scan, an independent method to experimentally obtain phase spaces. It is also demonstrated that tomography can work for time-resolved phase-space mapping and slice emittance measurement, given the right diagnostics. Finally, we review the results obtained in experiments at the University of Maryland using this generalized version of the tomography diagnostic.

The outline of this paper is as follows. In Sec. II we review the tomographic algorithm for beams with space charge. In Sec. III, we describe our approach to validate tomography through simulation. In Sec. IV we review a number of experiments conducted at the University of Maryland by using phase-space tomography. Finally, we present our conclusions in Sec. V.

[a)]Paper CI2 4, Bull. Am. Phys. Soc. **54**, 54 (2009).
[b)]Invited speaker.

II. TOMOGRAPHY THEORY

The goal of tomography is to reconstruct of a higher n-dimensional space from projections at a lower $(n-1)$ dimension. Suppose that $f(x,y)$ corresponds to a two-dimensional distribution that we wish to reconstruct. Let $\rho=x\cos\theta+y\sin\theta(0\leq\theta\leq\pi)$ be the equation of a line, L, that is at a distance ρ from the origin and forms an angle, θ, with the y-axis. Then, the line integral along L is defined as[21]

$$\hat{f}_\theta(\rho)=\int_L f(x,y)ds$$
$$=\int_{-\infty}^{\infty}\int_{-\infty}^{\infty}dxdyf(x,y)\delta(\rho-x\cos\theta-y\sin\theta). \quad (1)$$

The function $\hat{f}_\theta(\rho)$ is known as the Radon transform of the distribution $f(x,y)$. A projection of $f(x,y)$ is formed by combining a set of line integrals. The simplest projection is a collection of "parallel" line integrals, as is given by Eq. (1) for a fixed θ while ρ is varied. Such projections taken at various angles can be used to recover the original distribution via the Fourier backprojection algorithm (FBA).[21]

Below is an outline of the FBA method that we implemented. If $F(u,v)$ is the two-dimensional Fourier transform of the function $f(x,y)$, then its inverse Fourier transform is given by $f(x,y)=\int_{-\infty}^{\infty}\int_{-\infty}^{\infty}F(u,v)e^{j2\pi(ux+vy)}dudv$. By exchanging the rectangular coordinate system in the frequency domain (u,v) for a polar coordinate system (w,θ), the equation becomes $f(x,y)=\int_0^{\pi}\int_{-\infty}^{\infty}F(w,\theta)|w|e^{j2\pi w\rho}dwd\theta$. Using the Fourier slice theorem[21] we substitute the one-dimensional Fourier transform of the Radon transform at angle, θ, $S_\theta(w)=\int_{-\infty}^{\infty}\hat{f}_\theta(\rho)e^{-j2\pi w\rho}d\rho$, for the two-dimensional Fourier transform $F(w,\theta)$. Then,

$$f(x,y)=\int_0^{\pi}\int_{-\infty}^{\infty}S_\theta(w)|w|e^{j2\pi w\rho}dwd\theta. \quad (2)$$

Equation (2) is further simplified to

$$f(x,y)=\int_0^{\pi}Q_\theta(\rho)d\theta, \quad (3)$$

where Q is given by $Q_\theta(\rho)=\int_{-\infty}^{\infty}S_\theta(w)|w|e^{j2\pi w\rho}dw$ and is known as "filtered projection." Therefore, if several parallel projections corresponding to angles from 0 to π are known, the tomographic image can be reconstructed in two steps. First, the filtered projections Q are obtained; and, second, the resulting projections for each angle are added [using Eq. (3)] to generate an estimate of the distribution $f(x,y)$. The accuracy of the reconstruction will depend on the number of projections and the corresponding angular resolution between them.

Next, we relate the Radon transform to mapping the beam's phase space. Figure 1 illustrates a typical tomography experimental setup. Suppose that $\mu(y_0,y_0')_{z_0}$ and $\mu(y,y')_{z_1}$ are the phase-space distributions at two certain points, z_0 and z_1, along the beam line. In a linear system, the particle motion between the two positions obeys

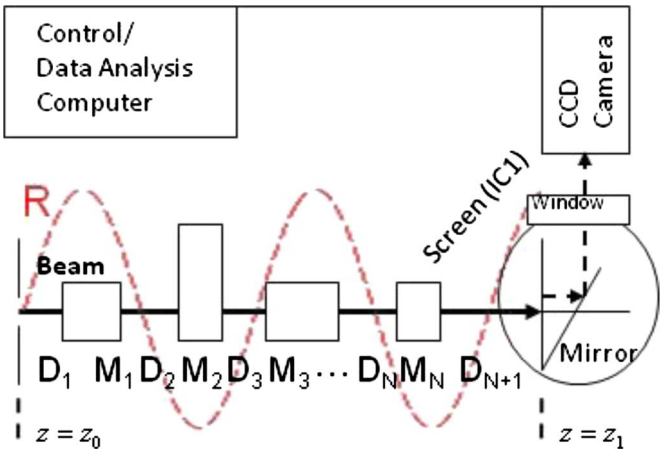

FIG. 1. (Color online) Schematic layout of the configuration for tomography, including orientation of the magnets and transfer matrices. The dashed line shows the evolution of the beam envelope.

$$\begin{pmatrix} y \\ y' \end{pmatrix}=T\begin{pmatrix} y_0 \\ y_0' \end{pmatrix}, \quad (4)$$

where $T=\begin{pmatrix} T_{11} & T_{12} \\ T_{21} & T_{22} \end{pmatrix}=\Pi_{i=1}^{N}D_{N+1}M_ND_NM_{N-1}D_{N-1}\cdots M_1D_1$ is the transport matrix. We note that M and D are the magnet and drift matrices, respectively. Placing a screen along the beam's path at z_1 provides a two-dimensional projection of the four-dimensional phase-space distribution $f(x,x',y,y')_{z_1}$, which is given by $g(x,y)_{z_1}=\int\int f(x,x',y,y')_{z_1}dx'dy'$. Integrating this distribution over x leads to the spatial beam profiles along y,

$$c(y)_{z_1}=\int g(x,y)_{z_1}dx$$
$$=\int\left(\int\int f(x,x',y,y')_{z_1}dxdy'\right)dx'. \quad (5)$$

McKee *et al.*[15] showed that a simple scaling equation relates those beam profiles to the Radon transform, $\hat{\mu}_{\theta,z_0}(\rho)$ of the transverse phase space $\mu(y_0,y_0')_{z_0}$. That is

$$\hat{\mu}_{\theta,z_0}(\rho)=\hat{\mu}_{\theta,z_0}(y/s)=sc(y)_{\theta,z_1}, \quad (6)$$

where s is the scaling factor given by[15] $s=\sqrt{T_{11}^2+T_{12}^2}$, and θ is the corresponding projection angle given by[15] $\tan\theta=T_{12}/T_{11}$. Therefore, by applying Eq. (6), tomographic techniques retrieve the transverse phase-space distribution of a beam using its projections in configuration space. Those projections can be obtained by varying the strength of the magnet upstream of the imaging screen which has the effect of rotating the distribution in phase space through an angle, θ.

In the presence of space-charge a complexity arises in calculating the transport matrix elements. Our approach is as follows. If we assume linear forces an expression similar to Eq. (4) can be formed but the elements of T will depend on the beam radius and beam position. This is because the net focusing strength now becomes $\kappa(z)=\kappa_0(z)-(K/R(z)^2)$, where κ_0 is the magnet's focusing strength, R is the $2\times$rms size of the beam envelope, and K is the generalized

perveance, a dimensionless quantity that is given by $K=2I/I_0(\beta^3\gamma^3)$, where I is the current and β and γ are the corresponding relativistic velocity and energy factors. Note that I_0 is the characteristic current, a constant, and equal to 17 kA for electrons. In order to obtain the R dependence with z we solve the KV envelope equations,[22]

$$R''(z) + \kappa_0(z)R(z) - \frac{K}{R(z)} - \frac{\varepsilon^2}{R(z)^3} = 0. \quad (7)$$

In order to solve Eq. (7), the assumed initial conditions at z_0 are crosschecked by comparing the calculated- and measured-beam sizes at z_1, the location of our screen. Should they not agree well, we adjust the initial conditions and repeat our envelope calculations until they reach agreement.

Once the evolution of R with respect to z is known, the net focusing function and the corresponding transport matrix are calculated by a superimposing many subelements.[23] Then, from the transport matrix, we determine the rotation angle and scaling factor, and finally apply Eq. (6) to obtain the phase-space projections for the tomography analysis.

III. PHASE-SPACE TOMOGRAPHY SIMULATION

The model proposed in the previous section assumed linear space-charge forces inside and outside the beam core, no emittance growth and negligible image forces. To test the accuracy of our algorithm, we simulated a tomography beam experiment using the electrostatic particle-in-cell code WARP.[24,25] The code simulates space-charge effects in 2-dimensional (2D) or 3-dimensional (3D) by advancing particles in a transverse slice under the impact of external forces and self-consistent self-fields. We used the x-y 2.5-D slice model of WARP that was shown to be accurate,[26] since the beam is elongated in z compared to the pipe's diameter, and varies little during its propagation over a longitudinal distance comparable to the beam's diameter. We employed a 512×512 grid for the Poisson solver, a step size of 2 mm along z, and 640 000 particles. In Sec. III A, we explore the accuracy of the tomography diagnostic on space-charge, and, in Sec. III B, we test the accuracy of tomography for different beam distributions. Note that in Refs. 23 and 27 we studied the effects of various errors in the reconstruction such as the angular reconstruction needed, the total angular span required, and the effect of uncertainties in magnet strength. For this discussion, it sufficient to say that a full 180° phase-space rotation with angular resolution less than 14° will assure a high-resolution phase-space map.

For our simulation, we select a magnet configuration that consists of two sets of alternating-gradient (FODO) sections, with four quadrupoles ($N=4$). The distance between the magnets centers is 16 cm. The simulation is initialized at $z=z_0$ which is located 8 cm upstream the center of the first quadrupole and the photos and phase spaces are generated at $z=z_1$ which is sited 5.3 cm downstream the fourth quadrupole. Simulating the tomography under that geometry gives us more confidence about its future applicability in the actual experiment (see Sec. IV). Unless stated otherwise, we assumed that the beam starts with a semi-Gaussian distribution, meaning that the particle density is uniform across it, and the velocity profile is Gaussian with a uniform temperature.

TABLE I. Simulated beam parameters.

χ	I (mA)	R (mm)	Total projections	Maximum angular step (deg)	Angular span (deg)
0.30	0.6	1.3	168	14.0	179.2
0.72	7	2.8	152	14.9	179.2
0.90	24	4.8	126	20	175.0

The procedure of the tomography simulation was as follows. For each quadrupole current setting, we ran a simulation, collected a snapshot of the beam's density in configuration space at $z=z_1$, and saved it. We applied the tomographic reconstruction to those simulated images to produce a phase space that we then compared with the actual phase space obtained directly from the simulation. The direct WARP phase space self-consistently includes nonlinear space charge and image forces. Thus, repeating this process for different initial beam distributions and for beams with different degrees of space charge intensity provided us with confidence in the technique.

A. Dependence of tomography accuracy on space-charge

To examine the effect of space charge on the reconstruction, we used three beams, each of different intensity. The content of space charge was quantified via the dimensionless intensity parameter $\chi=K/\kappa_0R^2$ (Ref. 28) that compares the contribution of the emittance and current terms on the rms envelope equation. Table I lists the intensity parameter, current, initial beam size, number of projections, maximum angular step between adjacent projections, and total angular span we used. Note that while varying the magnets' focusing strength, we selected the settings to ensure no beam losses. Due to the large beam sizes obtained while scanning the magnets for the 24 mA beam, the total phase space rotation was restricted to 175°; this was not a problem for the other two beams where a $\approx$180° phase space rotation was achieved.

The right and left columns in Fig. 2 are the tomographic- and WARP-generated phase spaces, respectively, for our three beams in increasing current order from top to bottom. The inset of the phase spaces indicates the $4\times$rms emittances from those phase spaces. All distributions are at $z=z_1$ and correspond to the case where the focusing strength for first and third quadrupole was set $\kappa_{0,1}=\kappa_{0,3}=-235.2\ \mathrm{m}^{-2}$ and the strength of the second and fourth quadrupole was set at $\kappa_{0,2}=\kappa_{0,4}=235.2\ \mathrm{m}^{-2}$. Due to the low current of the beam in Fig. 2(a), we neglected the space-charge forces in the tomographic analysis. This was not the case for the second [Fig. 2(b)] and third beam [Fig. 2(c)] where space charge was considered in the tomography-reconstruction process according to the procedure outlined in Sec. II.

Tomography accurately reconstructed the phase space for beams with a moderate content of space charge

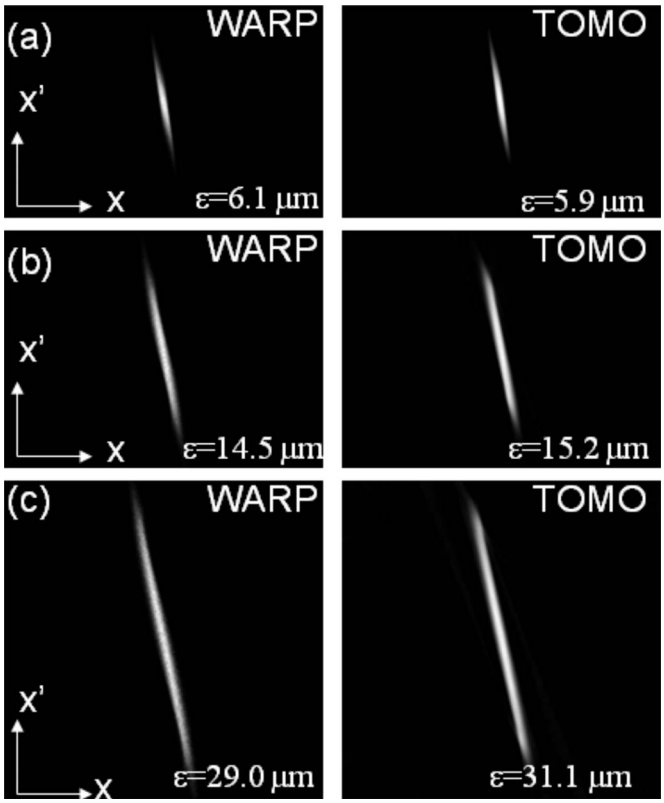

FIG. 2. Recovered phase spaces from WARP (left side), and tomography (right side) for beams with different intensity parameters: (a) $\chi=0.3$, (b) $\chi=0.72$, and (c) $\chi=0.9$.

($\chi \leq 0.72$) with an emittance error below 5%. The data for more intense beams ($\chi=0.9$) suggest a slightly higher percentage of error ($\approx 10\%$) but the agreement between tomography and simulation is still relatively good. This lower effectuality is likely due the substantial amount of space-charge that, in turn, might engender nonlinear forces not included in our analysis.

B. Dependence of tomography accuracy on initial beam distribution

In this section we study the effect of the initial distribution on the tomography reconstruction. Using two different distributions, we initiated our simulation at $z=z_0$ and reconstructed the phase space at $z=z_1$. To compare our findings, we assume that all the beams are equivalent in rms, meaning that they have the same current, energy, emittance, and size as the uniform 7 mA beam in Sec. I. The distributions explored here are the hollow velocity (uniform xy and hollow xx') and five beamlet and are shown in Figs. 3(a) and 3(b), respectively. Such distributions are of particular interest in beam physics. For example, a hollow-velocity distribution tends to be a general feature of thermionic gridded electron guns as has been observed experimentally and computationally.[29] Additionally, a multibeamlet distribution is suitable for heavy-ion applications,[30,31] where, instead of accelerating one beam it is advantageous to accelerate many and merge them before they hit the target.

The WARP-generated and tomography-reconstructed phase spaces are shown in Fig. 4, in the first and second column, respectively. These results indicate good agreement; this was true also for the five-beamlet distribution. It is interesting to note that even though such distribution introduces nonlinear space-charge forces, the linear tomography model proved surprisingly effective in reconstruction, with an error less than 7% in the emittance value.

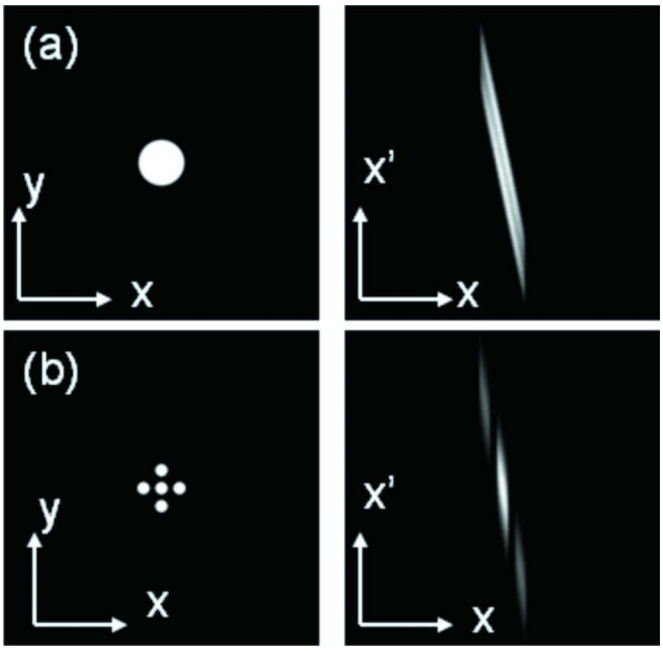

FIG. 3. (Color online) Beam distributions in configuration space (left) and in phase space (right) at $z=z_0$.

IV. TOMOGRAPHIC MEASUREMENT OF THE PHASE-SPACE EVOLUTION FOR SPACE-CHARGE DOMINATED BEAMS

A. Experimental configuration and available diagnostics

Some of the experiments were carried out on the University of Maryland Electron Ring (UMER) a 10 keV nonrelativistic ($\beta=v/c=0.2$) ring. The beam current is adjusted by an aperture plate at the exit of the anode, which has six different-sized round slots, including a five-beamlet mask. Following the plate is a 1.4 m-injection line containing one solenoid and six matching quadrupoles. The UMER ring consists of 18 sections each containing four quadrupoles and two dipoles, distributed over a 11.52 m circumference. The longitudinal profile of the beam was rectangular with 100 ns full width half maximum and an 8 ns rise time. The UMER configuration and its design parameters are detailed elsewhere.[25]

A fast Bergoz[32] current monitor installed immediately after the injector solenoid measured the longitudinal current profile of the beam. Two kinds of fluorescent screens were installed to map its transverse distribution: one was based on $Gd_2O_2S(Tb)$ with a 1.6 μs time response for time-integrated measurements and the second was a fast ZnO:Ga phosphor with decay time 2.4 ns for time-resolved measurements. The screens were placed in all but four sections housing the

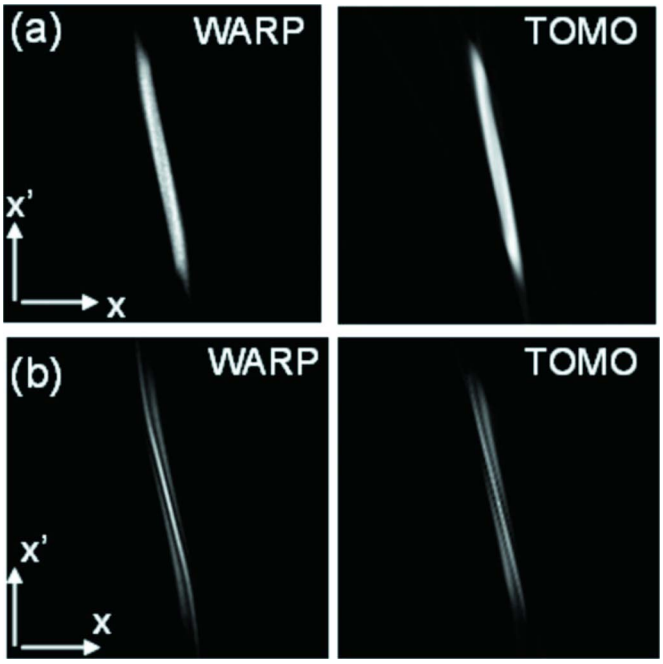

FIG. 4. (Color online) Phase spaces for the 7 mA as obtained by WARP (left column) and tomography (right column) at $z=z_1$ for two different input distributions.

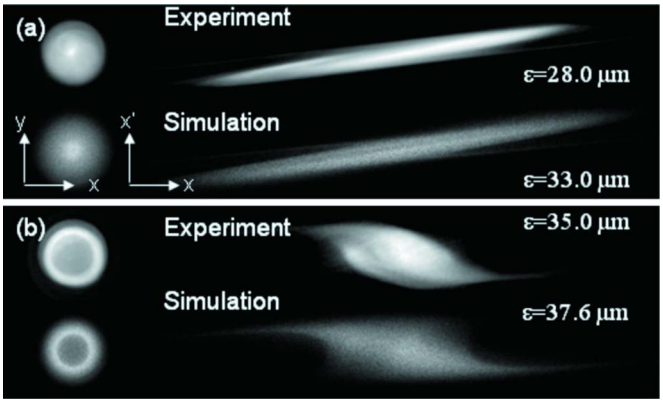

FIG. 5. (Color online) Comparison of the configuration space (left column) and phase space (right column), between experiment and simulation for two different magnet-pair settings. Top row corresponds to the measured distribution in experiment and bottom row shows the predictions from WARP simulation.

diagnostic chambers of UMER and one was installed downstream of the injector solenoid. The phosphor-screen image of the beam was reflected by a single surface mirror placed 45° to the screen; then, the beam could be monitored through a window. For time-resolved measurements, the beam images were captured by fully programmable intensified charge-couple device 16-bit camera (PIMAX2; Princeton Instruments Inc.).

We conducted further experiments on the long solenoid experiment (LSE), a linear system with solenoids serving as basic focusing magnets rather than the quadrupoles in UMER. The main transport line consisted of a thermionic gun, two solenoids (S1 and S2), a Bergoz coil, and a fast fluorescent screen. The solenoids were located 13.1 and 29.5 cm from the aperture, the coil was positioned between them, and the screen was placed 13.5 cm downstream of S2. The gun produced beams with energy from 1–5 keV. More details about the LSE configuration are in Ref. 27.

B. Tomography with solenoids

According to the literature, until 2007 all beam tomographic researches used only quadrupoles magnets to rotate the phase space. Since quadrupoles focus in one direction and defocus on the other, they generate large asymmetric beams and nonlinearities that may alter the results. Since solenoids afford more uniform focusing, it may be advantageous to use them in tomography. At University of Maryland, we completed a proof-of-principle experiment to benchmark solenoidal tomography on the LSE.[33]

Before the experiment, we verified the technique by simulating the process. Using the LSE configuration and following the procedure described in Sec. II, we ran numerous WARP simulations to generate the projections, and compared the phase-space obtained directly with that reconstructed from the data. We found that 48 scans were sufficient to attain a 180° phase-space rotation and produce phase-space images with a background noise below 5%. Our linear space-charge solenoidal tomography model proved its effectiveness in the reconstruction process with an error of less than 10% in the value of the rms emittance.[33]

The experimental procedure involved taking photos at the screen for each of 48 pairs of magnet strengths. The electron gun produced a 4 keV, 12 mA space-charge-dominated beam with a generalized perveance equal to 7.1×10^{-4}, and a non-normalized $4\times$rms emittance of 30 μm. Parts of our data are shown in Fig. 5; we give more results in Ref. 33. The pair settings of the solenoidal strengths we choose to reconstruct are 74.0 and 60.0 G [Fig. 5(a)] and 57.3 and 60.0 G [Fig. 5(b)] for S1 and S2, respectively. The first column corresponds to beam in configuration space as captured by the charge-coupled device (CCD) camera. To further benchmark solenoidal tomography, we compared our experimental findings with the WARP simulation; our results are also shown in Fig. 5. Note that both phase spaces indicate a hollow internal structure. These perturbations were absent when we replaced the initial hollow distribution in the simulation with a uniform one. Therefore, the hollowness we noted likely reflects an initial nonuniform distribution probably associated with the nonuniform emission from the gun cathode. We verified this fact later after the cathode was replaced.

C. Time-dependent phase-space tomography

In this section we demonstrate a proof-of-principle experiment to show the possibility of reconstructing the time-resolved-phase-space distribution by tomography. We obtain time-resolved phase-space maps for a parabolic beam bunch that is close to an ellipsoidal distribution. The time resolution is of the order of a few nanoseconds, i.e., much shorter than the beam bunch's length (50–100 ns), and therefore adequate for studying beam dynamics under our beam conditions.

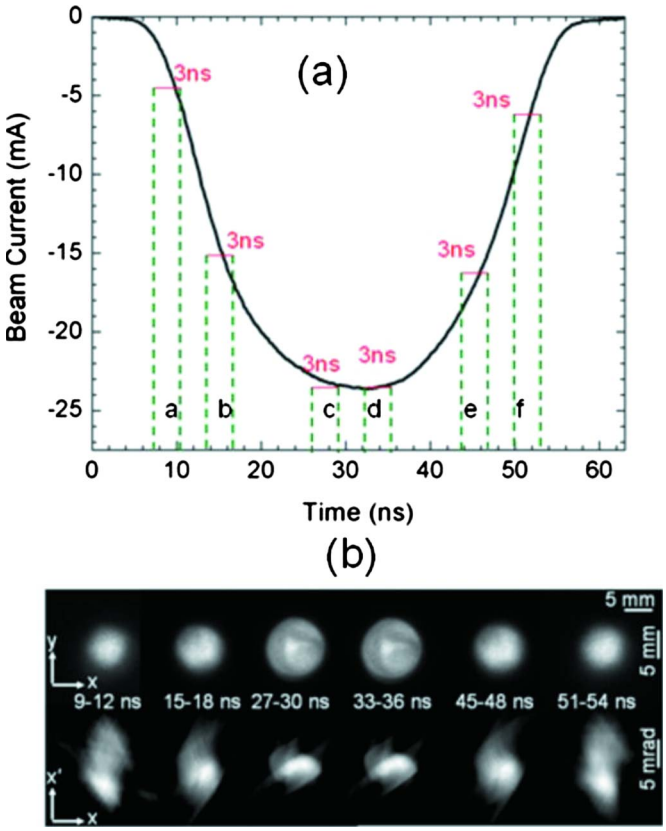

FIG. 6. (Color online) (a) Signal collected at the Bergoz coil showing the longitudinal current profile of the parabolic beam, indicating the approximate locations of the camera gates. (b) Beam in configuration space (top) and in phase space (bottom) for slices a, b, c, d, e, and f, reconstructed at LC1.

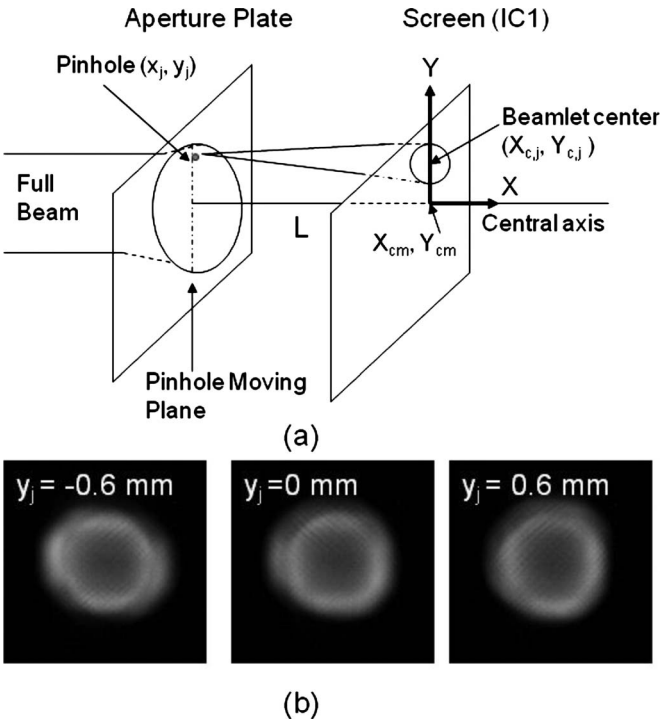

FIG. 7. Illustration of the principle of the pinhole-scan method.

The experiment[34] was carried out on the LSE, and to recover the phase space, the approach described in Sec. III B was employed. The only difference was the combined use of fast phosphor screens and an intensified charge-coupled device (ICCD)-gated camera to map the phase space in narrow (3–10 ns) longitudinal (time) slices within the beam pulse. For this experiment, the beam was pulsed at 60 Hz with energy 5 keV and a peak current equal to 23.5 mA. Figure 6(a) shows the longitudinal current profile from the signal at the Bergoz FCT, as well as the position of the slices used in the phase-space measurement (labeled with letters from a to f). A number of images at the screen (LC1), each corresponding to a 3 ns beam slice, were collected by setting the ICCD camera's gate window at 3 ns, and moving it progressively from the beam's head toward its tail. Figure 6(b) (top) shows the resulting beam distributions in configuration space for the six different slices (a, b, c, d, e, and f). Each photo resulted from 55 frame integrations. As the beam propagates, each slice will evolve differently in the transverse direction because it has a different current. Thus, in LC1, there will a variation of beam size within the pulse, as is clearly evident in the beam photos in Fig. 6(b).

Figure 6(b) (bottom) shows the measured phase space by tomography on the location of the screen. Both configuration-space images and the phase-space distributions reveal a detailed structure that differs from slice to slice. As discussed previously, part of the structure inside the phase space arises from the nonuniform emission from the gun cathode. Furthermore, like the configuration-space images, the phase spaces depend on their position along the beam; both exhibit symmetry at about the peak of the pulse.

D. Experimental verification of phase-space tomography

An independent measurement of the phase-space distribution was developed[35] by sweeping the smallest aperture (the pinhole), mounted on the large diameter aperture wheel at the exit of the UMER electron gun. The principle of the process is schematically shown in Fig. 7(a). Specifically, we can move the pinhole vertically (same x, different y) and thus can sample different parts of the full beam behind the pinhole. After exiting the gun, the beam passes through a solenoid and reaches a phosphor screen located downstream at $L=28.4$ cm. Figure 7(b) shows screen photos of individual beamlets for different pinhole positions y_j. The pinhole radius (0.25 mm) is much smaller than the beamlet radius on the screen (7 mm), so that the transverse position of each electron that reaches the screen is proportional to its transverse velocity at the pinhole's position. Thus, we can estimate the average angle of the beam at the pinhole, $\langle y' \rangle_j$, by recording the center Y_c of each of the individual beamlets.

A phase space can be generated tomographically by scanning the injector solenoid located just upstream the screen. Shown in Fig. 8(a) is the tomographically reconstructed phase space for the 23 mA beam. The filled dots in Fig. 8(b) depict the local average transverse-velocity versus horizontal position obtained from this plot. Specifically, we evaluated the line integral $\langle y' \rangle_j = \int dy' y' \mu(y=y_j, y')$ at different locations along the spatial direction of the reconstructed

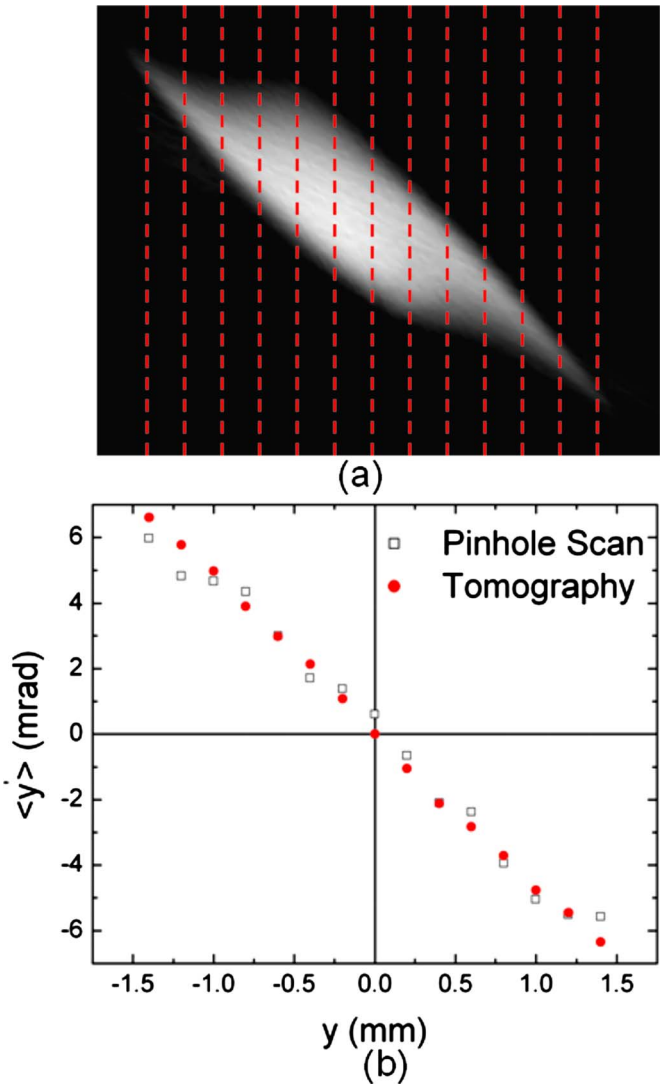

FIG. 8. (Color online) (a) Tomographically reconstructed phase space of the 23 mA beam at the aperture. (b) Variation in the local average transverse velocity obtained from (a) (filled cycles) as well as the pinhole scan (open squares).

phase space [see dotted vertical lines in Fig. 8(a)]. Depicted in the same plot by the open squares are the points generated by the pinhole scan. Interestingly, the pinhole scan data show a modulation of the centroid position at the same spatial period (i.e., 0.69 mm) as the anode grid wires which is most likely a result of the shadow of these wires as the pinhole is swept past them. Such modulation was not visible on the tomographic data that samples a vertically integrated phase space.

E. Phase mixing of intense beams

In this section we explore the mixing properties of charged particle beams by artificially constructing a distribution consisting of five distinct but nearby beamlets in a quincunx pattern. Such a distribution is of interest because, from Poisson's equation, it enhances greatly the radial nonlinearity of the self-fields. Also, it is of practical interest[36] because it relates to a class of transverse beam-combining lattice designs that were proposed[30,31,37] for achieving, economically, the high-current, low emittance beams required for HIF applications.

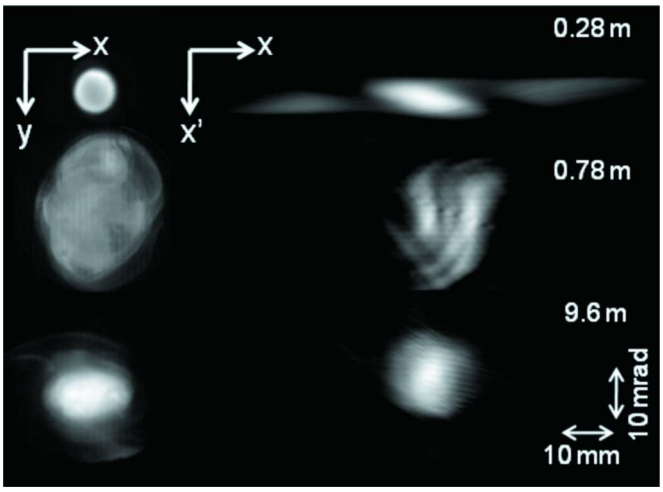

FIG. 9. (Color online) Evolution of a beam leaving a five-beamlet aperture at different locations inside the UMER ring in configuration space (left) and xx' phase space (right).

The experiment[38] was carried out on UMER, where the five-beamlet aperture was placed right at the exit of the gun. The beam emerging from the mask had a current of 28 mA measured by the Bergoz, and a rms normalized emittance, $\varepsilon_{i,n}$, of 4 μm, measured by tomography and verified with the pinhole scan. The beam parameters correspond to a generalized perveance, K, of 4.2×10^{-4} and an intensity parameter $\chi=0.70$, placing the beam in the space-charge-dominated regime.

Figure 9 (left) shows several fluorescent-screen pictures labeled with the distance from the UMER aperture. Figure 9 (right) shows the xx' phase-space distribution measured by tomography at the same locations. The images indicate that the beam core retains, over meters, an intricate dynamical structure. At 0.28 m although the original beamlet pattern is not visible in configuration space, the beamlets are separated in phase space. Focusing the beam implies a rotation of the phase space, so we expected to see a pattern that naturally alternates between appearing in configuration and in the velocity space. However, further downstream (9.6 m) this phase space-pattern erased, pointing to a mixing of the distribution. Simulations[38] suggested that this phase mixing is related to space charge and occurred faster as the beam intensity increased. Furthermore, both the simulation and experiment revealed an initial rapid growth of emittance that slowed down as the nonuniform distribution homogenized. The measured 10% total growth agreed with the predictions of the free-energy theory,[6] where emittance is expected to rise from the conversion of the excess field energy of a nonuniform beam into transverse kinetic energy.

Next, we examine the effect of the initial distribution on the downstream beam evolution. Specifically, in Fig. 10, we show several fluorescent screen pictures (left) and the corresponding phase spaces (right) taken for a beam with parameters comparable to the one with the five beamlets, but that initially is uniform. Noteworthily, as before we see structures

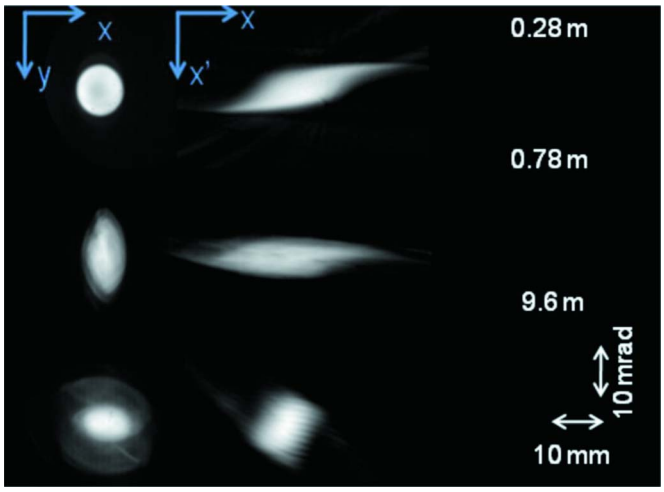

FIG. 10. (Color online) Evolution of a beam leaving a round aperture at different locations inside the UMER ring in configuration space (left) and xx' phase space (right). The beam intensity is comparable with that of the five beamlet in Fig. 9.

that are likely resulting from the imbalance of forces at the beam edge.[39] However, their evolution and mixing rates are different from the one seen with the five beamlets. As before we note the appearance of a halo that persists as the beam propagates through the focusing channel. WARP simulations indicated that the halo likely is a result of a small beam mismatch[6] and imperfections of the gun's geometry.[40]

V. SUMMARY

A model was presented to apply tomography to beams with space charge by assuming linear forces. The model was generalized to account for both solenoidal and quadrupole focusing lattices. The tomography algorithm was benchmarked against self-consistent simulation for both emittance and space-charge dominated beams. The diagnostic was also tested for beams with nonuniform distribution functions such as a five beamlet distribution, where space charge forces are initially nonlinear. It was found that the error increased with the beam intensity but for all cases remained below 10%. The algorithm was also verified experimentally by comparing its results with that obtained by a pinhole scan. Finally we experimentally demonstrated time-resolved phase-space mapping and slice emittance measurement, given a fast enough scintillator.

For phase-space tomography to be applicable to a wider range of accelerators, we foresee the following possible improvements. The approximation we make in this paper of linear forces everywhere does not adequately address the dynamics of halo particles straying far away from the beam core.[41] The algorithm also assumes a constant beam energy, a constraint that can be relaxed by using the appropriate transfer matrices for beams undergoing acceleration. The FBA described in this paper provides excellent reconstructions of phase space where we are capable of taking a large number of projections (50–100). Since the UMER screens are sufficiently robust, we have not looked into minimizing the number of projections needed for reconstruction. For high-energy ion beams with a relatively short scintillator lifetime such as the NDCX or SNS,[42] it is worthwhile to optimize this number, for instance, by using algebraic reconstruction algorithms.[21] We demonstrated time-resolved tomography in the nanosecond timescale, which is sufficient for the UMER beam. The technique should be extensible to faster timescales (e.g., picosecond) using appropriate diagnostics such as (prompt) optical transition radiation and a streak camera. Finally, solenoidal tomography for beams with nonzero canonical angular momentum would be necessary for applying the diagnostic to beams born within magnetic fields as in the case of flat-beam photoinjectors for linear colliders.[43]

ACKNOWLEDGMENTS

We wish to acknowledge D. Sutter, S. M. Lund, B. Beaudoin, D. Feldman, H. Li, C. Papadopoulos, and M. Walter for helpful discussions. The authors also wish to thank A. Woodhead for reading the paper and making useful suggestions.

This work is supported by the U.S. Department of Energy High Energy Physics and Fusion Energy Science and by the Department of Defense Office of Naval Research and Joint Technology Office.

[1] J. Wei, Y.-Y. Lee, D. Raparia, J. Sandberg, J. Tuozzolo, and W. T. Weng, Proceedings of the IEEE 2003 PAC Conference, Portland, OR, 2003 (unpublished), p. 571.
[2] R. B. Palmer, J. S. Berg, R. C. Fernow, J. C. Gallardo, H. G. Kirk, Y. Alexahin, D. V. Neuffer, S. A. Kahn, and D. J. Summers, Proceedings of the 2007 Particle Accelerator Conference, Albuquerque, NM (IEEE, New York, 2007), p. 3193.
[3] C. A. Brau, *Free Electron Lasers* (Academic, Oxford, 1990).
[4] G. H. Hoffstaetter and Y. H. Lau, Phys. Rev. ST Accel. Beams **11**, 070701 (2008).
[5] B. G. Logan, F. M. Bieniosek, C. M. Celata, J. Coleman, W. Greenway, E. Henestroza, J. W. Kwan, E. P. Lee, M. Leitner, P. K. Roy, P. A. Seidl, J.-L. Vay, W. L. Waldron, S. S. Yu, J. J. Barnard, R. H. Cohen, A. Friedman, D. P. Grote, M. Kireeff Covo, A. W. Molvik, S. M. Lund, W. R. Meier, W. Sharp, R. C. Davidson, P. C. Efthimion, E. P. Gilson, L. Grisham, I. D. Kaganovich, H. Qin, A. B. Sefkow, E. A. Startsev, D. Welch, and C. Olson, Nucl. Instrum. Methods Phys. Res. A **577**, 1 (2007).
[6] M. Reiser, *Theory and Design of Charge Particle Beams* (Wiley, New York, 1994), p. 183.
[7] R. C. Davidson, *Physics of Nonneutral Plasmas* (World Scientific, Singapore, 2001), p. 15.
[8] R. L. Gluckstern, Proceedings of the LINAC Conference, Fermilab, 1970 (unpublished), p. 811.
[9] S. M. Lund and R. C. Davidson, Phys. Plasmas **5**, 3028 (1998).
[10] E. P. Gilson, M. Chung, R. C. Davidson, M. Dorf, P. C. Efthimion, D. P. Grote, R. Majeski, and E. A. Startsev, Nucl. Instrum. Methods Phys. Res. A **577**, 117 (2007).
[11] N. H. Abel and J. Reine, J. Reine Angew. Math. **1**, 153 (1826).
[12] J. Radon, Ber. Saechs. Akad. Wiss. **69**, 262 (1917).
[13] O. R. Sander, R. A. Jameson, and R. D. Patton, IEEE Trans. Nucl. Sci. **26**, 3417 (1979).
[14] J. S. Fraser, IEEE Trans. Nucl. Sci. **26**, 1641 (1979).
[15] C. B. McKee, P. G. O'Shea, and J. M. J. Madey, Nucl. Instrum. Methods Phys. Res. A **358**, 264 (1995).
[16] M. Röhrs, C. Gerth, H. Schlarb, B. Schmidt, and P. Schmuser, Phys. Rev. ST Accel. Beams **12**, 050704 (2009).
[17] R. Connolly, R. Michnoff, T. Moore, T. Shea, and S. Tepikian, Nucl. Instrum. Methods Phys. Res. A **443**, 215 (2000).
[18] H. Li, "Control and transport of intense electron beams," Ph.D. dissertation, University of Maryland, College Park, 2004, pp. 102–117.

[19]V. Yakimenko, M. Babzien, I. Ben-Zvi, R. Malone, and X.-J. Wang, Phys. Rev. ST Accel. Beams **6**, 122801 (2003).
[20]A. Friedman, D. P. Grote, C. M. Celata, and J. W. Staples, Laser Part. Beams **21**, 17 (2003).
[21]A. C. Kak and M. Slaney, *Principles of Computerized Tomographic Imaging* (IEEE, New York, 1988), p. 49.
[22]F. J. Sacherer, IEEE Trans. Nucl. Sci. **18**, 1105 (1971).
[23]D. Stratakis, R. A. Kishek, H. Li, S. Bernal, M. Walter, B. Quinn, M. Reiser, and P. G. O'Shea, Phys. Rev. ST Accel. Beams **9**, 112801 (2006).
[24]D. P. Grote, A. Friedman, I. Haber, and S. Yu, Fusion Eng. Des. **32–33**, 193 (1996).
[25]R. A. Kishek, S. Bernal, C. L. Bohn, D. Grote, I. Haber, H. Li, P. G. O'Shea, M. Reiser, and M. Walter, Phys. Plasmas **10**, 2016 (2003).
[26]A. Kishek, S. Bernal, M. Reiser, M. Venturini, J. G. Wang, I. Haber, and T. F. Godlove, Nucl. Instrum. Methods Phys. Res. A **415**, 417 (1998).
[27]D. Stratakis, Ph.D. dissertation, University of Maryland, College Park, 2008.
[28]M. Reiser, P. G. O'Shea, R. A. Kishek, S. Bernal, P. Chin, S. Guharay, Y. Li, M. Venturini, J. G. Wang, V. Yun, W. Zhang, Y. Zou, M. Pruessner, T. Godlove, D. Kehne, P. Haldemann, R. York, D. Lawton, L. G. Vorobev, I. Haber, and H. Nishimura, Proceedings of the 1999 Particle Accelerator Conference, New York, NY (IEEE, New York, 2007), p. 234.
[29]I. Haber, S. Bernal, C. M. Celata, A. Friedman, D. P. Grote, R. A. Kishek, B. Quinn, P. G. O'Shea, M. Reiser, and J.-L. Vay, Nucl. Instrum. Methods Phys. Res. A **519**, 396 (2004).
[30]P. A. Seidl, C. M. Celata, A. Faltens, E. Henestroza, and S. A. MacLaren, Phys. Rev. ST Accel. Beams **6**, 090101 (2003).
[31]C. M. Celata, W. Chupp, A. Faltens, W. M. Fawley, W. Ghiorso, K. D. Hahn, E. Henestroza, D. Judd, C. Peters, and P. A. Seidl, Fusion Eng. Des. **32–33**, 219 (1996).
[32]Bergoz Instrumentation, Espace Allondon Ouest 01630 Saint Genis Pouilly, France.
[33]D. Stratakis, K. Tian, R. A. Kishek, I. Haber, M. Reiser, and P. G. O'Shea, Phys. Plasmas **14**, 120703 (2007).
[34]D. Stratakis, R. A. Kishek, R. B. Fiorito, K. Tian, I. Haber, P. G. O'Shea, M. Reiser, and J. C. T. Thangaraj, Phys. Rev. ST Accel. Beams **12**, 020101 (2009).
[35]D. Stratakis, R. A. Kishek, R. B. Fiorito, I. Haber, M. Reiser, and P. G. O'Shea, "Experimental verification of tomographic phase mapping with space-charge using a pinhole scan," J. Appl. Phys. (submitted).
[36]R. Noble and J. Spencer, Proceedings of the 2007 Particle Accelerator Conference, Albuquerque, NM (IEEE, New York, 2007), p. 3112.
[37]D. P. Grote, J. W. Kwan, and G. A. Westenskow, Nucl. Instrum. Methods Phys. Res. A **577**, 58 (2007).
[38]D. Stratakis, R. A. Kishek, I. Haber, S. Bernal, M. Reiser, and P. G. O'Shea, Phys. Rev. ST Accel. Beams **12**, 064201 (2009).
[39]S. Bernal, R. A. Kishek, M. Reiser, and I. Haber, Phys. Rev. Lett. **82**, 4002 (1999).
[40]I. Haber, S. Bernal, R. Feldman, R. A. Kishek, P. G. O'Shea, C. Papadopoulos, M. Reiser, D. Stratakis, M. Walter, A. Friedman, D. P. Grote, and J.-L. Vay, Proceedings of the 2007 Particle Accelerator Conference, Albuquerque, NM (IEEE, New York, 2007), p. 3564.
[41]S. M. Lund and B. Bukh, Phys. Rev. ST Accel. Beams **7**, 024801 (2004).
[42]F. M. Bieniosek, E. Henestroza, M. Leitner, B. G. Logan, R. M. More, P. K. Roy, P. Ni, P. A. Seidl, W. L. Waldron, and J. J. Barnard, Nucl. Instrum. Methods Phys. Res. A **606**, 146 (2009).
[43]P. Piot, Y.-E. Sun, and K.-J. Kim, Phys. Rev. ST Accel. Beams **9**, 031001 (2006).